INTERNATIONAL JOURNAL FOR NUMERICAL METHODS IN FLUIDS, VOL. 14, 423–441 (1992)

FINITE VOLUME COMPUTATION OF THE TURBULENT FLOW OVER A HILL EMPLOYING 2D OR 3D NON-ORTHOGONAL COLLOCATED GRID SYSTEMS

P. J. COELHO AND J. C. F. PEREIRA

Instituto Superior Técnico/Universidade Técnica de Lisboa, Mechanical Engineering Department, Pavilhão de Máquinas, 1º Andar, Av. Rovisco Pais, 1096 Lisboa Codex, Portugal

SUMMARY

A general numerical method for the solution of the complete Reynolds-averaged Navier–Stokes equations for 2D or 3D flows is described. The method uses non-orthogonal co-ordinates, Cartesian velocity components and a pressure–velocity-coupling algorithm adequate for non-staggered grid systems. The capability of the method and the overall performance of the k–ε eddy viscosity model are demonstrated by calculations of 2D and 3D flow over a hill. Solution error estimations based on fine grids, e.g. 320 × 192 control volumes, together with comparisons with standard turbulence model modifications, low-Reynolds-number or streamline curvature effects, have allowed the investigation of model drawbacks in predicting turbulent flows over surface-mounted hills.

KEY WORDS Finite volume method Non-orthogonal co-ordinates Turbulent recirculating flow

1. INTRODUCTION

The understanding and capability of calculating turbulent separated flows on streamlined surfaces are relevant for a wide range of problems in industrial and environmental engineering. The flow over a convex/concave surface such as a hill presents strong favourable and adverse pressure gradients, streamline curvature with stabilizing and destabilizing effects on turbulence, a detachment line that is not fixed, contrary to flows over sharp edges, and very high velocity gradients in the near-wall region on the top of the hill. These effects raise questions on the adequacy of the turbulence model assumptions used in different flow regions[1–3] as well as on the numerical accuracy of the flow predictions. In addition, 3D effects may occur in nominally two-dimensional separated turbulent shear flows (see e.g. Reference 4).

For flows involving complex geometries a body-fitted co-ordinate system should be used. Several formulations of the equations have been applied (see e.g. References 5–7). In this work a strong conservation form of the equations is used together with non-staggered non-orthogonal grid systems. Predictions are reported for 2D and 3D confined turbulent flow over a hill and compared with experimental values at the centre channel plane.[8] Non-staggered grid systems are preferred because there is only one set of control volumes, which simplifies the code. Furthermore, the pressure–velocity-decoupling problem is not overcome by the use of staggered grid if curvilinear co-ordinates are used. In order to ensure pressure–velocity coupling in a non-staggered grid system, the pressure-weighted interpolation method was used (see e.g. Reference 7).

0271–2091/92/040423–19$09.50

Received February 1991
Revised May 1991

The aim of this work is to validate the general numerical method developed for the solution of the complete Reynolds-averaged Navier–Stokes equations. The numerical solution errors are estimated with a technique based on Richardson extrapolation[9, 10] and sufficiently fine grids are employed to ensure numerically accurate and nearly grid-independent results. Moreover, unlike most previous predictions of separated flows that have been conducted for flows over sharp edges, the present flow configuration adds a case study to the literature that will assist the understanding of the performance of the standard k–ε eddy viscosity model for wall-bounded separated flows.

Numerical predictions of turbulent flow over hills are scarce but are of great relevance for a wide range of turbulent separated flows (see e.g. the review article by Simpson[11]). Specific objectives of this work are: comparison of 2D and 3D predictions at the central plane; comparison of the predictions obtained with wall functions and the low-Reynolds-number k–ε model; comparison of the standard k–ε and a streamline curvature correction model.

Section 2 presents the equations and the discretization procedure. In Section 3 detailed comparisons with the available experimental data are made after a detailed investigation of the numerical accuracy of the results. A discussion of the results is presented in Section 4 and the paper ends with summary conclusions.

2. THE MATHEMATICAL FORMULATION

2.1. *Governing equations*

The governing equations expressing conservation of mass and momentum can be written in a co-ordinate-free form as

$$\frac{\partial \rho}{\partial t}+\operatorname{div}(\rho \mathbf{v})=0, \tag{1}$$

$$\frac{\partial}{\partial t}(\rho \mathbf{v})+\operatorname{div}(\rho \mathbf{v}\otimes \mathbf{v})=\operatorname{div}\mathbf{T}+\mathbf{S}_v, \tag{2}$$

where the stress tensor for a Newtonian fluid is given by

$$\mathbf{T}=\mu[\operatorname{grad}\mathbf{v}+(\operatorname{grad}\mathbf{v})^{\mathrm{T}}]-(p+\tfrac{2}{3}\mu\operatorname{div}\mathbf{v})\mathbf{I}. \tag{3}$$

In these equations ρ is the density, μ is the dynamic viscosity, p is the static pressure, $\mathbf{v}$ is the velocity vector and $\mathbf{I}$ is the second-order unit tensor. The source term $\mathbf{S}_v$ accounts for the body forces.

Depending on the choice of the velocity components (e.g. Cartesian, covariant or contravariant components), there are different choices for splitting the vectorial momentum equation (2). Here the Cartesian components are used, leading to the following form of the momentum conservation equation:

$$\frac{\partial}{\partial t}(\rho u_i)+\operatorname{div}(\rho \mathbf{v} u_i)=\operatorname{div}\mathbf{t}_i+S_{u_i}, \tag{4}$$

where u_i is the Cartesian velocity component along direction i with base vector $\mathbf{i}_i$ and $\mathbf{t}_i$ is given by

$$\mathbf{t}_i=\mathbf{T}\cdot\mathbf{i}_i=\mu\,[\operatorname{grad}u_i+(\operatorname{grad}\mathbf{v})^{\mathrm{T}}\cdot\mathbf{i}_i]-(p+\tfrac{2}{3}\mu\operatorname{div}\mathbf{v})\,\mathbf{i}_i. \tag{5}$$

When the divergence operator is expressed in the strong conservation form, the governing equations (1) and (4) can be written as

$$\frac{\partial \rho}{\partial t}+\frac{1}{J}\frac{\partial}{\partial \xi^j}(\rho u_k \beta_k^j)=0, \tag{6}$$

$$\frac{\partial}{\partial t}(\rho u_i)+\frac{1}{J}\frac{\partial}{\partial \xi^j}(\rho u_k \beta_k^j u_i)=\frac{1}{J}\frac{\partial}{\partial \xi^j}(t_{ki}\beta_k^j)+S_{u_i}, \tag{7}$$

where

$$\beta_k^j=J\frac{\partial \xi^j}{\partial x^k}, \tag{8}$$

$$t_{ki}=\frac{\mu}{J}\left(\frac{\partial u_i}{\partial \xi^m}\beta_k^m+\frac{\partial u_k}{\partial \xi^m}\beta_i^m\right)-(p+\tfrac{2}{3}\mu \operatorname{div}\mathbf{v})\delta_{ki}. \tag{9}$$

A repeated index denotes summation over the three spatial components. The non-orthogonal co-ordinate system (ξ^1, ξ^2, ξ^3) and the Cartesian co-ordinate system (x^1, x^2, x^3) are related by the co-ordinate transformation $x^i=x^i(\xi^j)$ whose Jacobian is denoted by J.

Since the flow under consideration is turbulent, the common approach of Reynolds velocity decomposition was used. The momentum conservation equation in time-averaged form appears as

$$\frac{\partial}{\partial t}(\rho\overline{u_i})+\frac{1}{J}\frac{\partial}{\partial \xi^j}(\rho\overline{u_k}\beta_k^j\overline{u_i})=\frac{1}{J}\frac{\partial}{\partial \xi^j}[(\overline{t_{ki}}-\rho\,\overline{u_k'u_i'})\beta_j^k]+S_{\overline{u_i}}, \tag{10}$$

where the overbar denotes a mean value and the fluctuating components are identified by the turbulent Reynolds stress tensor $\overline{u_k'u_i'}$. Closure of the equations requires a turbulence model and in this study the well-known k–ε eddy viscosity turbulence model[12] and a low-Reynolds-number k–ε turbulence model[13] were used. In this first-order closure the Reynolds stresses are expressed by a turbulent viscosity and Boussinesq approximation yielding the following relationship in tensor notation:

$$-\rho\,\overline{u_k'u_i'}=\frac{\mu_t}{J}\left(\frac{\partial\overline{u_i}}{\partial \xi^m}\beta_k^m+\frac{\partial\overline{u_k}}{\partial \xi^m}\beta_i^m\right)-\tfrac{2}{3}(\rho k+\mu_t \operatorname{div}\mathbf{v})\delta_{ki}. \tag{11}$$

The turbulent viscosity μ_t is defined as

$$\mu_t=C_\mu f_\mu \rho\frac{k^2}{\varepsilon}, \tag{12}$$

where C_μ and f_μ are constants of the model, k is the turbulent kinetic energy and ε is the dissipation rate. Transport equations are solved for these two quantities.

The complete set of equations to be solved for a steady, incompressible, turbulent flow can be written (the overbars are dropped for simplicity) in the form

$$\frac{\partial}{\partial \xi^j}(\rho u_k \beta_k^j)=0, \tag{13}$$

$$\frac{\partial}{\partial \xi^j}(\rho u_k \beta_k^j u_i)=\frac{\partial}{\partial \xi^j}\left[\frac{\mu_t+\mu}{J}\left(\frac{\partial u_i}{\partial \xi^m}\beta_k^m\beta_k^j+\frac{\partial u_k}{\partial \xi^m}\beta_i^m\beta_k^j\right)\right]-\frac{\partial}{\partial \xi^j}(p\beta_i^j)+JS_{u_i}, \tag{14}$$

$$\frac{\partial}{\partial \xi^j}(\rho u_k \beta_k^j k)=\frac{\partial}{\partial \xi^j}\left[\frac{1}{J}\left(\frac{\mu_t}{\sigma_k}+\mu\right)\frac{\partial k}{\partial \xi^m}\beta_k^m \beta_k^j\right]+J(G-\rho\varepsilon), \tag{15}$$

$$\frac{\partial}{\partial \xi^j}(\rho u_k \beta_k^j \varepsilon)=\frac{\partial}{\partial \xi^j}\left[\frac{1}{J}\left(\frac{\mu_t}{\sigma_\varepsilon}+\mu\right)\frac{\partial \varepsilon}{\partial \xi^m}\beta_k^m \beta_k^j\right]+J\left(C_1 f_1 \frac{\varepsilon}{k} G-C_2 f_2 \rho \frac{\varepsilon^2}{k}\right), \tag{16}$$

where μ stands for the laminar viscosity. The generation of turbulent kinetic energy G can be expressed as

$$G=\frac{\mu_t}{J^2}\left(\frac{\partial u_i}{\partial \xi^m}\beta_j^m+\frac{\partial u_j}{\partial \xi^m}\beta_i^m\right)\left(\frac{\partial u_i}{\partial \xi^m}\beta_j^m\right). \tag{17}$$

Standard values were assigned to all the constants of the k–ε model $(C_\mu, C_1, C_2, \sigma_k, \sigma_\varepsilon)$[14] for which f_μ, f_1 and f_2 are equal to unity. When the low-Reynolds-number model is used the constants C_μ, C_1, C_2, σ_k and σ_ε remain the same and f_μ, f_1 and f_2 are chosen according to the model proposed by Lam and Bremhorst[13] as listed in Table I.

2.2. Discretization procedure

The finite volume/finite difference method is used to discretize the governing equations (13)–(16) over a non-staggered mesh. These equations can be written in the form of a general transport equation for discretization purposes as

$$\frac{\partial}{\partial \xi^j}(\rho u_k \beta_k^j \phi)=\frac{\partial}{\partial \xi^j}\left(\frac{\Gamma_\phi}{J}\frac{\partial \phi}{\partial \xi^m}\beta_k^m \beta_k^j\right)+S_\phi. \tag{18}$$

Table II lists the contributions of Γ_ϕ and S_ϕ for each ϕ-equation.

Table I. Functions for the low-Reynolds-number k–ε turbulence model

$f_\mu = [1-\exp(-0{\cdot}0165\,R_y)]^2 \times (1+20{\cdot}5/R_T)$
$f_1 = 1+(0{\cdot}05/f_\mu)^3$
$f_2 = 1-\exp(-R_T^2)$
$R_T = \rho k^2/\mu\varepsilon$
$R_y = \rho k^{1/2} y/\mu$

Table II. Diffusion coefficients and source terms of the governing equations

ϕ	Γ_ϕ	S_ϕ
1	0	0
u_i	$\mu+\mu_t$	$\frac{\partial}{\partial \xi^j}\left(\frac{\mu+\mu_t}{J}\frac{\partial u_k}{\partial \xi^m}\beta_i^m \beta_k^j - p\beta_i^j\right)+JS_{u_i}$
k	$\frac{\mu_t}{\sigma_k}+\mu$	$J(G-\rho\varepsilon)$
ε	$\frac{\mu_t}{\sigma_\varepsilon}+\mu$	$J\left(C_1 f_1 \frac{\varepsilon}{k} G-C_2 f_2 \rho \frac{\varepsilon^2}{k}\right)$

The transport equation (18) is integrated over each control volume in the computational domain (see Figure 1) and the Gauss divergence theorem is applied. The convective term is discretized as

$$\int_V \frac{\partial}{\partial \xi^j}(\rho u_k \beta_k^j \phi)\,\mathrm{d}V = F_e\phi_e - F_w\phi_w + F_n\phi_n - F_s\phi_s + F_d\phi_d - F_u\phi_u, \tag{19}$$

where subscripts e, w, n, s, d and u stand for east, west, north, south, downstream and upstream cell faces respectively. The mass flux through the east face, for example, is given by

$$F_e = \rho_e(u_1\beta_1^1 + u_2\beta_2^1 + u_3\beta_3^1)_e, \tag{20}$$

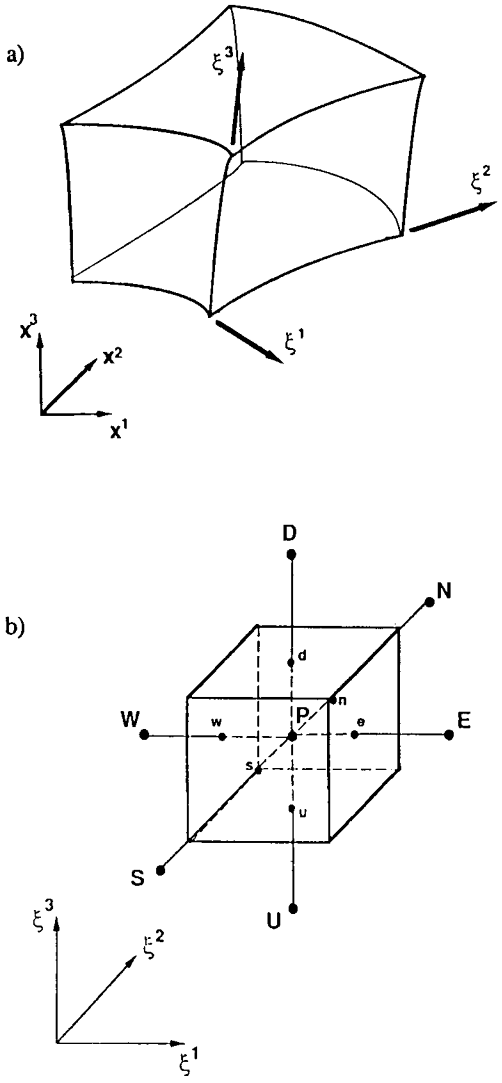

Figure 1. Typical control volumes: (a) physical domain; (b) computational domain

where it is assumed that $\Delta\xi^i = 1$. In order to calculate the values of the dependent variable at the cell faces, the hybrid central/upwind convection discretization scheme[15] was used. Although the scheme induces a truncation error that leads to 'artificial numerical diffusion', this could be minimized in the present study by the use of non-orthogonal grids (small velocity skewness with grid lines) and a large number of control volumes.

The discretization of the diffusion term yields

$$\int_V \frac{\partial}{\partial\xi^j}\left(\frac{\Gamma_\phi}{J}\frac{\partial\phi}{\partial\xi^m}\beta_k^m\beta_k^j\right)\mathrm{d}V = I_\mathrm{e}^\mathrm{D} - I_\mathrm{w}^\mathrm{D} + I_\mathrm{n}^\mathrm{D} - I_\mathrm{s}^\mathrm{D} + I_\mathrm{d}^\mathrm{D} - I_\mathrm{u}^\mathrm{D}, \tag{21}$$

where

$$I_\mathrm{e}^\mathrm{D} = \left(\frac{\Gamma_\phi}{J}\right)_\mathrm{e}\left(\frac{\phi_\mathrm{E}-\phi_\mathrm{P}}{\Delta\xi^1}(\beta_k^1\beta_k^1)_\mathrm{e} + \frac{(\phi_\mathrm{n}-\phi_\mathrm{s})_\mathrm{e}}{\Delta\xi^2}(\beta_k^2\beta_k^1)_\mathrm{e} + \frac{(\phi_\mathrm{d}-\phi_\mathrm{u})_\mathrm{e}}{\Delta\xi^3}(\beta_k^3\beta_k^1)_\mathrm{e}\right)\Delta\xi^2\,\Delta\xi^3, \tag{22}$$

and similarly for the other faces. Since $\Delta\xi^i = 1$ and

$$J\Delta\xi^1\,\Delta\xi^2\Delta\xi^3 = \delta V, \tag{23}$$

where δV is the cell volume in the physical domain, equation (22) can be simplified as

$$I_\mathrm{e}^\mathrm{D} = \left(\frac{\Gamma_\phi}{\delta V}\right)_\mathrm{e}(\phi_\mathrm{E}-\phi_\mathrm{P})(\beta_k^1\beta_k^1)_\mathrm{e} + \left(\frac{\Gamma_\phi}{\delta V}\right)_\mathrm{e}[(\phi_\mathrm{n}-\phi_\mathrm{s})_\mathrm{e}(\beta_k^2\beta_k^1)_\mathrm{e} + (\phi_\mathrm{d}-\phi_\mathrm{u})_\mathrm{e}(\beta_k^3\beta_k^1)_\mathrm{e}]. \tag{24}$$

The first term represents a normal derivative and the others are cross-derivatives that are explicitly incorporated in the source term.

The pressure term is discretized as follows, taking for example the momentum conservation equation for velocity component u_1:

$$\int_V \frac{\partial}{\partial\xi^j}(p\beta_1^j)\,\mathrm{d}V = (p_\mathrm{e}-p_\mathrm{w})(\beta_1^1)_\mathrm{P} + (p_\mathrm{n}-p_\mathrm{s})(\beta_1^2)_\mathrm{P} + (p_\mathrm{d}-p_\mathrm{u})(\beta_1^3)_\mathrm{P}, \tag{25}$$

where subscript P refers to the central grid node P.

The source terms in equations (13)–(16) are integrated following standard discretization practices:

$$\int_V S_\phi\,\mathrm{d}V = \left(\frac{S_\phi}{J}\right)_\mathrm{P}\delta V. \tag{26}$$

The discretized transport equation is obtained after assembling all the terms discretized above to yield the algebraic equation

$$a_\mathrm{P}\phi_\mathrm{P} = \sum_i a_i\phi_i + b, \tag{27}$$

where the summation extends over the neighbours of grid node P. The coefficients a_i are related to the convection and diffusion fluxes and the coefficient b accounts for the contribution of the source term.

2.3. Pressure–velocity coupling

When non-staggered grids are used and the velocity components at the cell faces are calculated using linear interpolation, decoupling between pressure and velocities can occur leading to spurious pressure oscillations. During the last decade several alternatives have been devised to avoid this problem.

The method described by Rhie and Chow[16] to avoid pressure–velocity decoupling is used in the present work and underrelaxation is introduced following the recommendations of References 17–20. In this method the velocity at a cell face (east, for example) is calculated as

$$u_{ie}^{*}=\alpha_{u_i}\overline{\left(\frac{\sum_k a_k(u_i)_k+b'-(p_n-p_s)\beta_i^2-(p_d-p_u)\beta_i^3}{a_P}\right)}_e-\alpha_{u_i}\left(\frac{\beta_i^1}{a_P}\right)_e(p_E-p_P)+(1-\alpha_{u_i})u_{ie}^{old}. \tag{28}$$

Here α_{u_i} is the underrelaxation factor for the velocity u_i and b' is the source term of the discretized momentum equation which does not include the pressure terms that were written explicitly. The overbar denotes a linear interpolated value between grid nodes P and E (see Figure 1). It can be seen that the cell face velocity depends on the pressures at the two neighbouring nodes as in the staggering practice and this is the reason why coupling between pressure and velocities is ensured.

The well-known SIMPLE algorithm was used with minor modifications arising from the use of non-staggered grids (see Reference 19 for details).

In the derivation of the pressure correction equations the pressure gradients along the cell face, arising from non-orthogonality of the grid lines, were neglected. This is a common approach which has been analysed recently by Peric.[21] He concluded that provided the departure from non-orthogonality is not too severe, it is computationally more efficient to neglect the non-orthogonality terms. Another common procedure is to include the cross-derivative diffusion fluxes in the source term of the discretized equations. These terms arise from non-orthogonality of the grid lines and so this approach can lead to an increase in CPU time when the skewness of the grid lines is significant.

The two aforementioned simplifications were made because they do not affect the solution accuracy and they lead to discretized equations which involve only seven coefficients relating the variable value at grid node P with its six closest neighbours. The solution of these equations was carried out by the strongly implicit method.[22,23] Convergence is achieved when the normalized absolute residual sums decrease below a given level, taken as 10^{-3} for all the dependent variables.

2.4. *Flow configuration and numerical grid generation*

The water flow configuration over a two-dimensional hill is presented in Figure 2. The hill height is $H=28$ mm and the base length is equal to $3{\cdot}85H$. The two-dimensional hill spans a channel of $6{\cdot}07H$ width and $7{\cdot}1H$ height. The hill blockage ratio is 1 : 7·1 and the aspect ratio (hill height/channel width) is 1 : 6. The relatively low aspect ratio may induce flow three-dimensionality, which will be numerically investigated in the next sections.

Measurements in this water tunnel, which was made with Perspex walls to allow optical access, were obtained[8] for $Re_H=6\times10^4$. Velocity was measured by a laser–Doppler velocimeter operated in the dual-beam, forward-scatter mode with sensitivity to the flow direction provided by light frequency shifting from acousto-optic modulation (Bragg cells). In the experiments the number of individual velocity values used to form the averages was always above 10 000 and the largest statistical errors are estimated to be 0·5 and 3% respectively for the mean and variance values.

For three-dimensional fluid flow configurations the physical domain is discretized in control volumes bounded by six faces and defined by the co-ordinates of the eight vertices. Several numerical grid generation techniques can be used for this purpose.[24] One of the most popular techniques consists of the solution of a system of elliptic Poisson equations. The source terms of these equations can be used to control the location of the grid nodes and there are several different proposals regarding the choice of the source terms.[24] This method could easily be

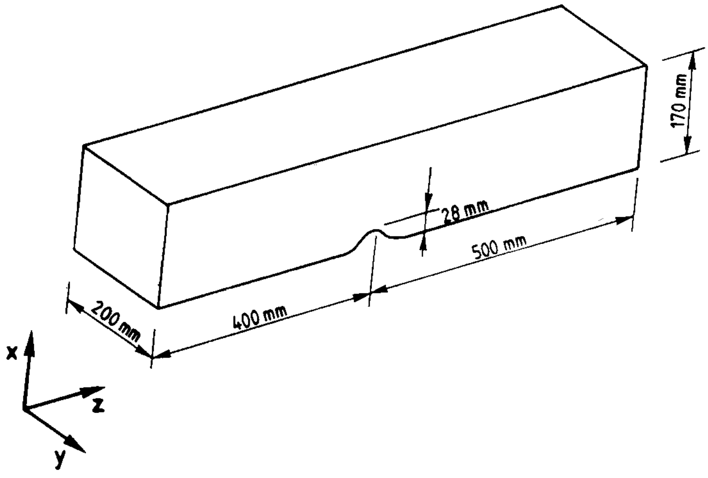

Figure 2. Geometry of turbulent flow over a hill

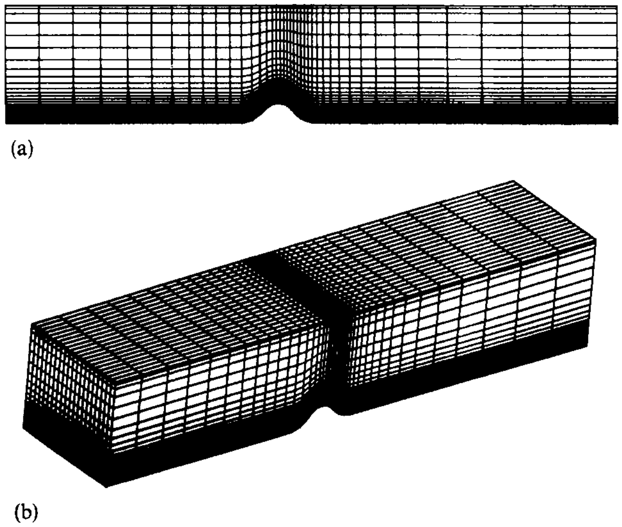

Figure 3. Typical meshes: (a) 2D flow (40 × 30 grid nodes); (b) 3D flow (40 × 30 × 20 grid nodes)

applied here as well. However, in this work an algebraic grid generation was preferred in order to allocate easily high-mesh-density regions as well as changing the grid spacing in order to conduct error estimation analysis. Although this could be done using an elliptic grid generator, it is simpler to apply an algebraic grid generation technique.

The boundary points at the lower and upper channel walls are selected and connected by straight lines. The distribution of points along the x-direction is chosen in order to concentrate the grid nodes in steep-velocity-gradient regions. The grid generated is repeated for each y = constant plane. In the computational domain each control volume is a cube with $\Delta\xi^1 = \Delta\xi^2 = \Delta\xi^3 = 1$. Figures 3(a) and 3(b) show examples of non-orthogonal grids for two- and three-dimensional configurations respectively.

2.5. *Boundary conditions*

The inlet boundary was located 14·3*H* upstream of the centre of the hill. At this section the influence of the hill may be neglected and fully developed turbulent flow conditions prevail. The inlet boundary conditions were prescribed according to the experimental data for undisturbed flow.[8] For three-dimensional calculations the inlet quantities were taken from the measurements[25] obtained in the entire channel cross-section without the hill. Dissipation of the turbulent kinetic energy was estimated based on hydraulic channel radius as the length scale. At the outlet section, located 18*H* downstream of the top of the hill, zero gradient was assumed for all dependent quantities.

The near-wall flow region was carefully investigated. Two approaches were followed. The first corresponds to the basic standard wall function approach where the wall fluxes for the wall-parallel velocities are calculated according to Launder and Spalding,[14] assuming in the first control volume close to the wall a logarithmic velocity profile, a constant-stress layer and local equilibrium of the turbulence. The convective and diffusive wall fluxes for turbulent kinetic energy are set to zero and production rates are calculated from the wall shear stresses evaluated from the wall function. The dissipation rate is calculated by integration of production. At the nodal points close to the wall the dissipation rate equation was not solved and ε-values were prescribed according to local equilibrium (i.e. the production rate of turbulent kinetic energy equals its dissipation rate).

The second approach does not use wall functions; instead the 'low-Reynolds-number' k–ε model was employed (see e.g. Reference 1). The Lam–Bremhorst model[13] was used by including the damping effect functionals listed in Table I in equations (12) and (16). This model requires a high grid resolution close to the wall. At the inlet plane 30 grid nodes in the vertical direction were used to cover the region $0 \leqslant y^+ \leqslant 50$, where the non-dimensional co-ordinate y^+ is defined as $U_\tau y/\nu$. The turbulent quantities up to $y^+ = 80$ were taken from the non-dimensionalized equilibrium boundary layer data presented by Patel *et al.*[2]

3. RESULTS

3.1. *Error estimation analysis*

Calculations using the standard k–ε model were performed with five different grids: 40×30, 80×60, 160×120, 160×240 and 320×192 grid nodes in the z- and x-direction respectively. The sensitivity of the numerical solutions to grid refinement is examined by comparing the predicted location of the separation and reattachment points for each grid (see Figure 4). The results show that the location of the separation point is in close agreement with the experimental data (shown by the horizontal line) for the three finer meshes. The predicted length of the recirculation zone increases with grid refinement approaching the experimental recirculation length.

A grid consisting of 160×200 control volumes was considered for the calculations using the low-Reynolds-number model. It yields a very good prediction of the reattachment point location but separation seems to occur too close to the top of the hill. The experimental separation point is estimated from the axial velocity measured 1 mm from the wall. When the low-Reynolds-number model is used, the distance from the first row of nodes to the wall is about 0·01 mm ($3{\cdot}5 \times 10^{-4} H$) and this explains the observed difference. If the predicted separation point were estimated from a row of nodes at a distance of 1 mm from the wall, the separation point location would be in excellent agreement with the experimental data. Hence the low-Reynolds-number model leads to a better prediction of the length of the recirculation zone than do standard wall functions. However, as will be analysed in Section 4, this is not a general conclusion.

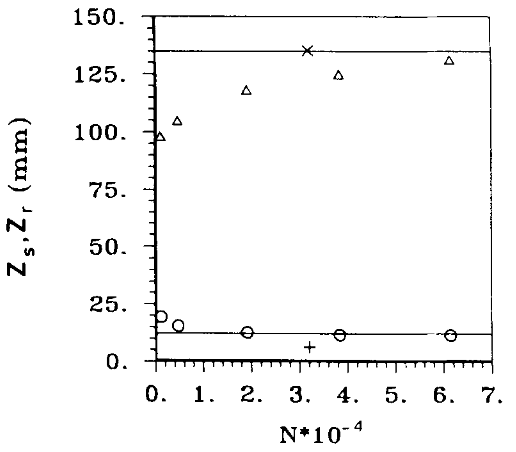

Figure 4. Prediction of location of separation (Z_s) and reattachment (Z_r) points as a function of number of grid nodes (N) (○, △, standard k–ε model; +, ×, low-Reynolds-number model; ——, experimental data)

As mentioned in Section 1, the numerical accuracy of the results was carefully investigated. The strategy used in this work follows the proposed standard technique of performing calculations on a sequence of refined grids, retaining the same discretization scheme.[10,26,27] Comparing error estimation and false diffusion errors, it has been found[27] that numerical errors can be high even in regions where false diffusion is not significant, owing to the transport of false diffusion errors. Therefore the following analysis is based on error estimation. Solution error estimation was carried out by Richardson extrapolation, comparing the numerical solutions obtained with 80×60 and 160×120 control volumes. The solution errors are proportional to the difference between solutions on two consecutive grids as shown in Figure 5(a) for the streamwise velocity field. The contours represent the values of $|W_h - W_{2h}|/W_0$, where W_h and W_{2h} are the streamwise velocities on the finer and coarser meshes respectively and W_0 is the mean bulk velocity at the inlet plane. The contour values are a measure of the local solution error on the finer grid (160×120). It can be seen that errors up to 10% are concentrated in a region close to the separation point. However, in the major part of the computational domain the solution errors do not exceed 5%. A similar analysis conducted on 160×98 and 320×192 grid systems yielded similar error contours but with maximum errors of 5%. The solutions obtained with 320×192 control volumes were considered to be satisfactory to distinguish the numerical errors from turbulence closure assumptions in the predictions.

The error estimation analysis conducted for turbulent kinetic energy (for meshes with 80×60 and 160×120 grid nodes), non-dimensionalized by the maximum value of k calculated on the fine grid, yields a maximum error smaller than 20% (see Figure 5(b)). This is much smaller than the large estimated errors found by Kessler *et al.*[10] for the flow around a surface-mounted square obstacle. This may be explained by the different body configuration and by the use of non-orthogonal grid co-ordinates, which decrease the velocity vector skewness with the grid lines and so decrease numerical false diffusion. The same estimation based on non-dimensionalization by W_0^2 rather than by maximum k yields negligible errors.

The above solution error estimation suggests that numerical diffusion is not a major error source owing to the high number of grid points used (320×192) and that the comparison between

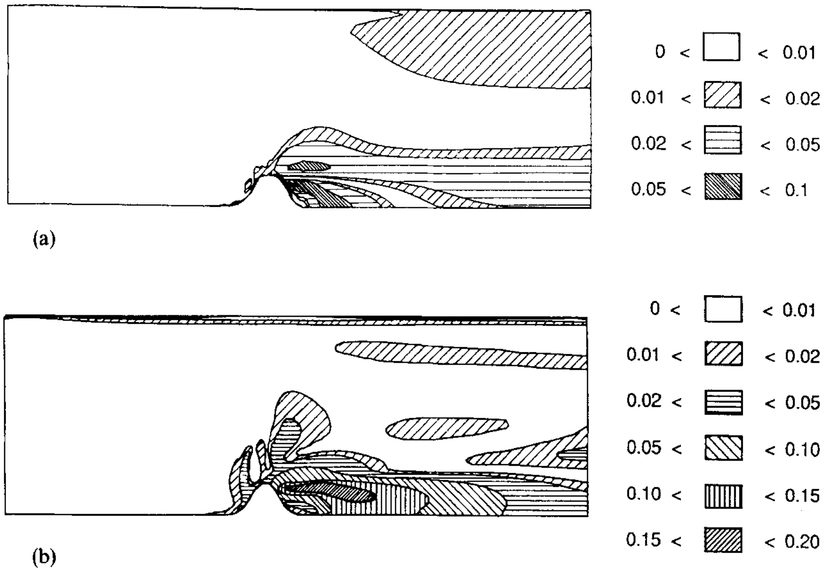

Figure 5. Contours of estimated solution errors: (a) streamwise velocity; (b) turbulent kinetic energy

predictions and measurements which follows may be interpreted as a test for the performance of the turbulence model assumptions used to predict this complex flow.

3.2. Comparison between two- and three-dimensional flow predictions

The motivation for investigating three-dimensional effects on the flow at the centre channel plane arises from the rather small aspect hill ratio of 1 : 6 reported in the measurements. The value of 1 : 10 was recommended by de Brederode and Bradshaw^{28} for flows over sharp edge, sudden discontinuity surfaces to avoid three-dimensional effects at the centre channel plane.

Calculations were carried out with a coarse grid ($80 \times 60 \times 20$) and compared with 2D predictions obtained with the same grid (80×60) in the z–x-plane. For comparison purposes it is important to carry out 3D predictions using exactly the same grid in the z–x plane as for the 2D predictions. The 3D predictions show that close to the bottom surface the flow is three-dimensional in the separated flow region. Figure 6(a) shows the predicted detachment and reattachment lines across the channel. The corner flow close to the side walls interacts strongly with the low-momentum streamwise flow, yielding a smaller separated flow region than at the centre channel plane.

Figure 6(b) shows profiles of the streamwise velocity component across the channel from the side wall to the centre channel plane at several distances from the bottom at $z/H = 2{\cdot}5$. The figure shows that for $x/H < 0{\cdot}2$ the flow presents a large region where three-dimensional effects are important but they do not contaminate the centre plane. This can also be concluded from Figure 6(c), where the streamwise velocity at the nearest grid point close to the wall is displayed as a surface plot. Although the flow is strongly affected by the side walls, it remains almost two-dimensional at the centre plane, as can be inferred from the comparison between 2D and 3D predictions for the streamwise and normal velocity component profiles shown in Figure 6(d).

Despite the implications of secondary channel flows driven by turbulence and side wall effects (see e.g. Reference 29), one can conclude that the 3D predictions using the k–ε eddy viscosity

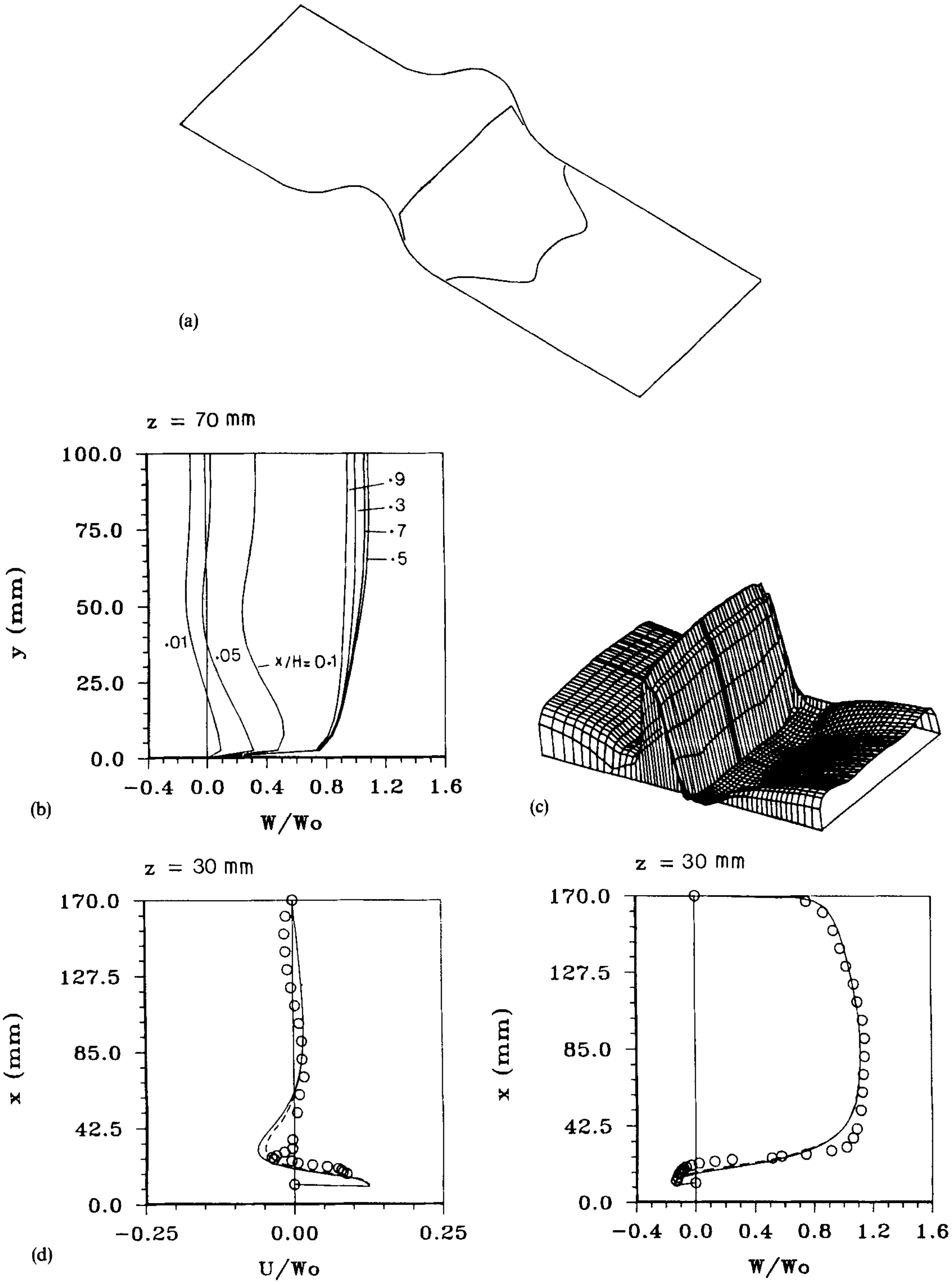

Figure 6. Results of three-dimensional computations: (a) location of separation and reattachment points; (b) spanwise profiles of streamwise velocity; (c) perspective of predicted streamwise velocity; (d) comparison of 2D and 3D predictions with experimental data (○, experimental data; ——, 2D predictions; – – –, 3D predictions)

model at the centre plane are virtually identical to the 2D predictions. Thus the remaining predictions that follow were obtained with a two-dimensional flow assumption.

3.3. Comparison between 'low-Reynolds-number' and wall function near-wall treatments

All the predictions that follow were obtained with a mesh comprising 320 × 192 grid nodes for the k–ε wall function treatment and with a 160 × 200 grid for the low-Reynolds-number k–ε model. The grid density corresponding to 320 × 192 was very high in the shear layer region, while for the low-Reynolds-number predictions this occurs in the near-bottom-wall region. Figure 7 shows the computed streamlines. The flow separates at $z/H = 0{\cdot}43$ and reattaches at $z/H = 4{\cdot}64$ and therefore the length of the separated flow region is well predicted within 5% compared with the measurements. When standard wall functions are used, the recirculation length is also well predicted.

There are still questions about how very small geometrical inaccuracies in the experimental configuration may induce relevant fluid flow perturbations or modifications. The very high number of grid nodes close to the surface used with the low-Reynolds-number k–ε model is adequate to analyse the above influences. With such a high number of grid nodes the shape of the hill is described very well and the polygonal contour obtained by joining the points on the boundary matches the curvilinear shape of the hill with an error less than or equal to $10^{-4}H$. Therefore the departure of the computed hill shape from the actual hill shape can be neglected for all practical purposes. Figure 8 shows the hill surface details taken from a careful inspection of the

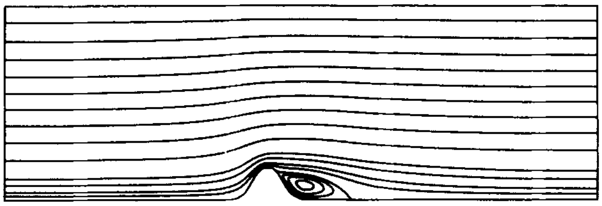

Figure 7. Streamlines of 2D flow over a hill

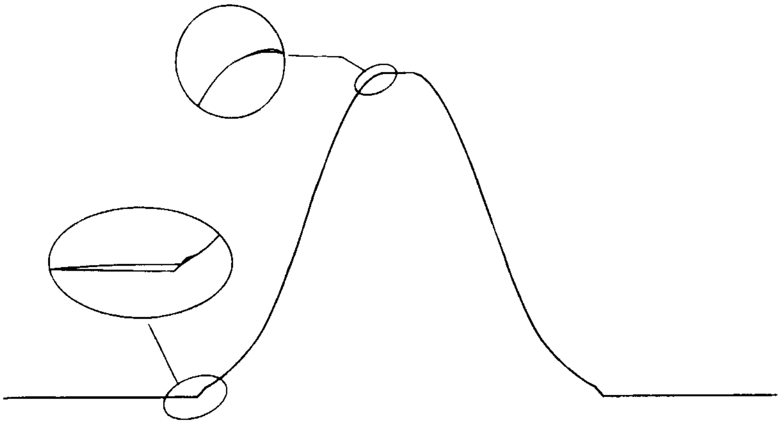

Figure 8. Details of recirculation regions predicted by low-Reynolds-number model (enlarged scale in vertical direction)

two-dimensional hill surface used in the experimental investigation.[8] The low-Reynolds-number predictions display three microscopic separated flow regions. Although these regions cannot be detected experimentally (they are of the same order of magnitude as the laser beam control volumes), they are expected physically and are a consequence of the non-smooth transition between the surface of the hill and the bottom wall and also of the shape of the curved surface at the top of the hill. The height of the sharp edge at the base of the hill is negligible compared to the hill height but high enough compared to the dimensions of the control volumes in the x-direction ($x/H = 3{\cdot}5 \times 10^{-4}$, 10 μm close to the wall). Consequently, the presence of the sharp edge is felt when using a very large number of control volumes in the near-wall region as required by a low-Reynolds-number turbulence model.

The convergence criterion for the predictions obtained with the low-Reynolds-number model was the same as for the wall function predictions, although the number of iterations required to achieve normalized residuals for mass and momentum smaller than 10^{-3} has almost doubled.

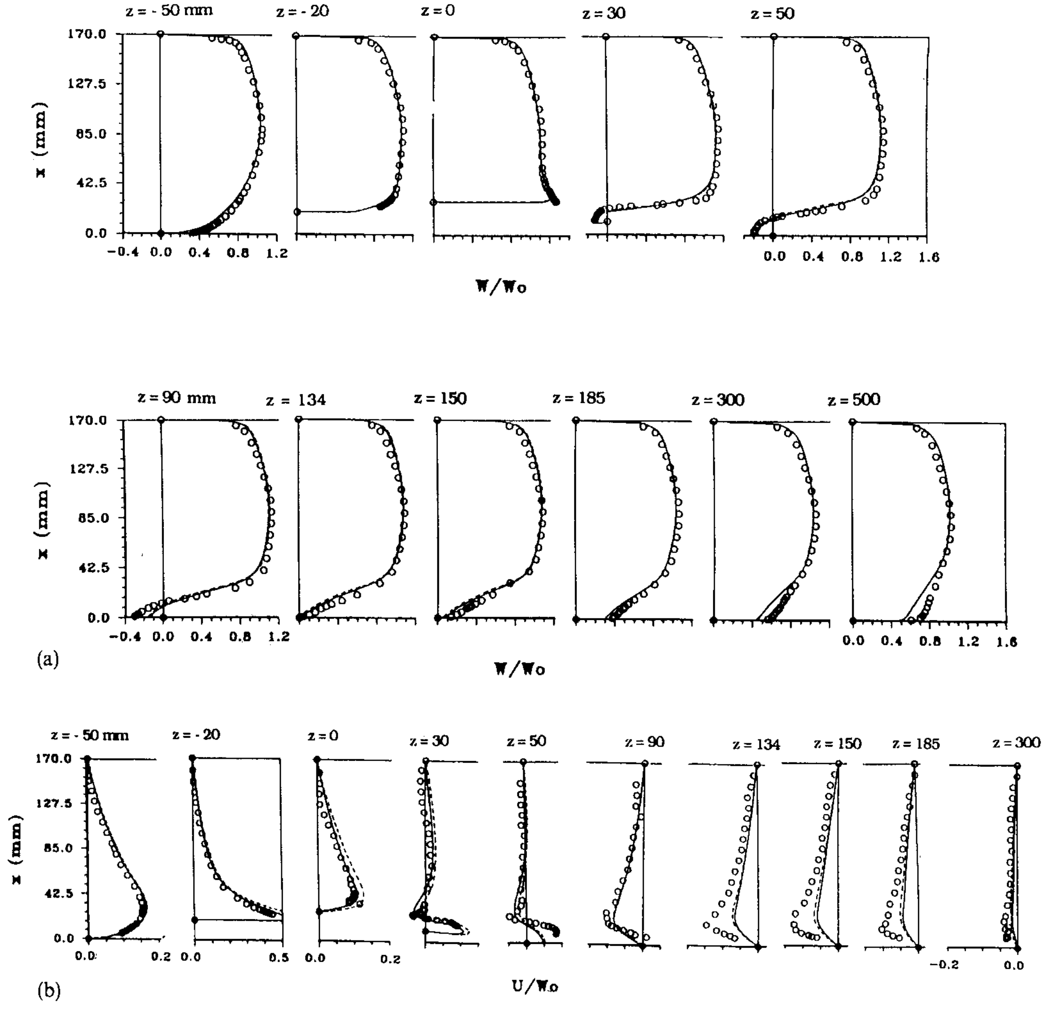

Figure 9. Comparison of predicted and measured velocity profiles (○, experimental data; ——, standard k–ε model; – – –, low-Reynolds-number model): (a) streamwise velocity; (b) crosswise velocity

Figures 9(a) and 9(b) show the streamwise and normal velocity predictions obtained with wall functions and the low-Reynolds-number model at different stations from $z/H = -1{\cdot}78$ to $17{\cdot}8$. Both k–ε model near-wall versions yield virtually identical results in the main flow region. Relatively large differences were obtained close to the wall, where the predicted friction coefficient with wall functions was higher than that predicted by the low-Reynolds-number model. The predicted mean velocity components are in good agreement with the measurements, except on the top of the hill where the data display a deeper velocity gradient and after the reattachment point where the predictions display too slow a recovery to fully developed channel flow.

The normal and shear stress predictions are shown in Figures 10(a)–10(c). Although the profile shapes are identical, very large discrepancies are depicted in the figures and some of them (strong underprediction of shear stresses surrounding the separated flow region) are not expected comparing the performance of the k–ε eddy viscosity with other turbulent shear flow predictions.

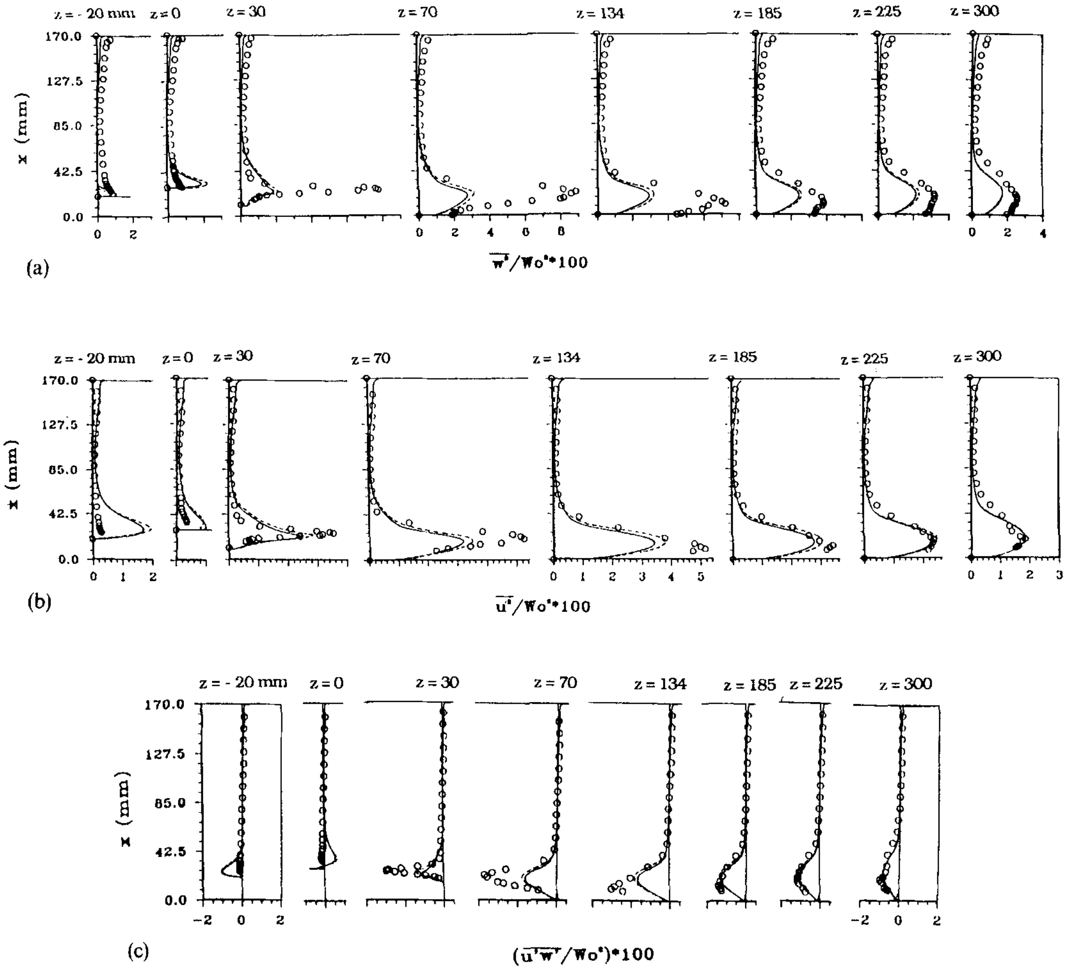

Figure 10. Comparison of predicted and measured turbulent quantities (○, experimental data; ——, standard k–ε model; - - -, low-Reynolds-number model): (a) streamwise normal stress; (b) crosswise normal stress; (c) shear stress

4. DISCUSSION

It is important to mention that the agreement between mean flow predictions and experiments presented in Figures 9(a) and 9(b) is surprisingly good compared with other separated shear flows (e.g. step flow and obstacle flow,[30,31] disk flow[32]). It is well known that the empirical wall function formulae do not scale well at reattachment and inside separated flow regions (see e.g. Reference 11); neither can the low-Reynolds-number model used predict correctly the effects of adverse pressure gradients on shear layers (see e.g. References 1, 2 and 33) or the ε-distribution in the near-wall region.[34,35] The good agreement between the wall function and low-Reynolds-number k–ε near-wall treatments suggests that near-wall turbulent characteristics do not play an important role in this flow configuration and that there is a rather weak dependence of the overall flow field on the near-wall region.

Figures 10(a)–10(c) show the normal and shear stress predictions. The profiles display an underprediction of momentum diffusion in the shear layer around the separated flow region (shear and normal stresses), contrary to the predictons of backward-facing step flow (see e.g. Reference 30). However, the turbulent transport of momentum after the reattachment point is satisfactorily predicted, but there is still significantly slower flow recovery in this region. Thus the k–ε eddy viscosity predictions are not in agreement with other similar separated shear flows and the results suggest that the physics of the flow is not well kept.

According to Thompson and Whitelaw[36] and Simpson,[11] immediately upstream of the mean flow separation the pressure gradient and convective terms dominate, with the components of the normal momentum equation tending in magnitude to those of the streamwise momentum equation as separation is approached. Under adverse pressure gradient conditions the model is expected to produce too large length scales at the reattachment point. Inside the separated flow region, turbulent diffusion is important in the streamwise momentum equation and is almost balanced by the pressure gradient. The same occurs in the k-equation, where production is small and diffusion is balanced by dissipation. Figures 10(a)–10(c) show that inside and surrounding the separated flow region there is a strong underprediction of normal and shear stresses. The importance of normal and shear stresses would suggest an overprediction in the reattachment length. This does not occur and a possible explanation may be attributed to the role of the normal momentum equation. By careful inspection of Figures 9(b) and 10(b) and assuming that the pressure gradient is of the same order of magnitude in the two momentum equations, the balance between normal stress terms and pressure gradient should be correct in the normal momentum equation. Thus the normal velocity component is satisfactorily predicted, as is the streamwise component inside the separated flow region. The magnitude of the turbulent stresses is incorrect but their gradient is correct.

In the downstream reattachment region the slower recovery to fully developed flow cannot be attributed to the shear stresses, which are satisfactorily predicted (see Figure 10(c)). In this region the momentum equation budget implies that convection is balanced by momentum diffusion, which is well predicted (see Figure 10(c)). However, the two convective terms are important immediately after reattachment owing to the high normal velocities close to the wall. The convective term $\partial\rho uw/\partial x$ is underpredicted because the normal velocity profile after reattachment is underpredicted (see Figure 9(b)). As a consequence the streamwise velocity component profiles display a much slower recovery towards developed conditions. It is interesting to note that in this region the good agreement shown in Figures 10 (a) and 10(c) between predictions and measurements is obtained by an overestimation of turbulent viscosity and an underestimation of mean strain rates, which is in agreement with a length scale overestimation close to reattachment. The same slower recovery to fully developed velocity profiles has been reported in a wide variety

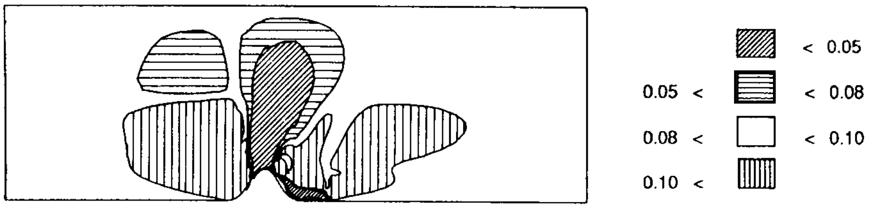

Figure 11. Contours of C_μ predicted with k–ε turbulence model with streamline curvature correction

of separated flows (e.g. second-order momentum closure predictions of obstacle flow,[31] large-eddy simulation of backward-facing step flow[37]).

The above discussion has ignored the contribution of streamline curvature to the turbulence field. Strong boundary-induced streamline curvature is expected with destabilizing effects on the convex regions and stabilizing effects on the concave regions. To include these effects in the k–ε eddy viscosity model, the C_μ-functionalization proposed by Leschziner and Rodi[38] was used. Although such functionalization was developed for axisymmetric flows, a similar derivation can be easily made for 2D planar flows. The final C_μ-function does not change provided that similar assumptions are used in its derivation. Contours of the predicted C_μ-values are shown in Figure 11 that clearly agree with the above streamline curvature influence on the turbulence field via eddy viscosity. Owing to lack space, we do not present all the predictions again. The main conclusions of the above predictions may be summarized as follows: up to the top of the hill the C_μ-functionalization has improved the predictions of mean and turbulent quantities but fails completely to improve the flow field in the separated region. The increases in the shear and normal stresses have consequently decreased the back flow in the streamwise velocity profiles and increased the maximum negative velocities very close to the wall. Thus the streamline curvature modification did not bring the mean flow predictions closer to the data after the detachment point as in other curved flows (see e.g. Reference 39).

Finally, the present test case has shown that the k–ε eddy viscosity model has produced satisfactory predictions of the mean velocity field, though it has not represented either the turbulent flow structure or the physics of the flow. As described by Simpson[11] and Goldberg and co-workers,[40,41] the mechanisms of turbulence near detachment within separated regions and reattachment are not conveyed by either the k–ε eddy viscosity or most other currently used turblence models. The present predictions have clearly reduced the numerical errors and we have tried to propose a new test case for numerical methods and turbulence models with the aim that it will receive similar attention to backward-facing step flow. The present predictions should be compared with 2D and 3D second-moment closures to give additional understanding of the physics and modelling aspects of the flow.

The numerical method presented can be applied directly to real hills of any shape. The inclusion of an energy equation is required to treat stratified flow problems. However, the accuracy of turbulence models for stratified flows is outside the scope of this paper.

5. CONCLUSIONS

A numerical method for the solution of the complete Reynolds-averaged Navier–Stokes equations for general two- or three-dimensional incompressible flows has been presented. The method uses non-orthogonal co-ordinates while retaining the velocity components in a Cartesian co-ordinate system at the centre of a non-staggered grid.

Calculations were performed for the flow over a hill. The following conclusions could be derived.

- (i) Solution error estimation analysis proved that very fine grids are required to decrease numerical errors. The maximum number of control volumes used (320 × 190) yielded maximum errors for the velocity components of around 5%.
- (ii) Although the present flow configuration presents an aspect ratio of 1:6, no three-dimensional effects on the centre channel plane were predicted by the k–ε eddy viscosity model.
- (iii) Predictions obtained with the wall function and low-Reynolds-number model near-wall treatments yield virtually identical results.
- (iv) The flow around a hill induces convex/concave streamline curvature. The C_μ-functionalization used to take into account streamline curvature effects on turbulence did not prove to be useful after the detachment point.
- (v) Surprisingly, the k–ε eddy viscosity model predictions yield good comparisons with the experimental separation length and mean flow field. However, the model could not capture the physics of the flow concerning the turbulent field.

REFERENCES

1. W. Rodi and G. Scheurer, 'Scrutinizing the k–ε turbulence model under adverse pressure gradient conditions', *ASME J. Fluids Eng.*, **108**, 174–179 (1986).
2. V. C. Patel, W. Rodi and G. Scheurer, 'Turbulence models for near-wall and low-Reynolds number flows: a review', *AIAA J.*, **23**, 1308–1319 (1985).
3. P. Bradshaw, 'Effects of streamline curvature on turbulent flows', *AGARDograph* **169**, 1973.
4. M. P. Jaroch and H. H. Fernholz, 'The two-dimensional character of a nominally two-dimensional separated turbulent shear flow', *J. Fluid Mech.*, **163**, 283–322 (1989).
5. I. A. Demirdzic, A. D. Gosman, R. I. Issa and M. Peric, 'A calculation procedure for turbulent flow in complex geometries', *Comput. Fluids*, **15**, 251–273 (1987).
6. H. C. Chen, V. C. Patel and S. Ju, 'Solutions of Reynolds-averaged Navier–Stokes equations for three-dimensional incompressible flows', *J. Comput. Phys.*, **88**, 305–336 (1990).
7. M. H. Kobayashi and J. C. F. Pereira, 'Calculation of incompressible laminar flows on non-staggered non-orthogonal grids', *Numer. Heat Transfer*, Part **B**, **19**, 243–262 (1991).
8. G. P. Almeida, D. F. G. Durão and M. V. Heitor, 'The recirculating flow in the wake of bidimensional hills', *Proc. 5th Int. Symp. on Application of Laser Techniques to Fluid Mechanics*, Lisbon, July 1990, Paper 4.2.
9. S. C. Caruso, J. H. Ferziger and J. Oliger, 'Adaptive grid techniques for elliptic flow problems', *Report TF-23*, Thermoscience Division, Stanford University, 1985.
10. R. Kessler, M. Peric and G. Scheuerer, 'Solution error estimation in the numerical predictions of turbulent recirculating flows', *AGARD CP-437*, 1988, Paper 9-1.
11. R. L. Simpson, 'Two-dimensional turbulent separated flow', *AGARDograph 287*, 1985.
12. W. P. Jones and B. E. Launder, 'The prediction of laminarization with a two-equation model of turbulence', *Int. J. Heat Mass Transfer*, **15**, 301–314 (1972).
13. C. K. G. Lam and K. A. Bremhorst, 'Modified form of the k–ε model for predicting wall turbulence', *J. Fluids Eng.*, **103**, 456–460 (1981).
14. B. E. Launder and D. B. Spalding, 'The numerical computation of turbulent flows', *Comput. Methods Appl. Mech. Eng.*, **3**, 269–289 (1974).
15. D. B. Spalding, 'A novel finite-difference formulation for differential expressions involving both first and second derivatives', *Int. j. numer. methods eng.*, **4**, 551–559 (1972).
16. C. M. Rhie and W. L. Chow, 'Numerical study of the turbulent flow past an airfoil with trailing edge separation', *AIAA J*, **21**, 1525–1532 (1983).
17. M. Majumdar, 'Role of underrelaxation in mometum interpolation for calculation of flow with non-staggered grids', *Numer. Heat Transfer*, **13**, 125–132 (1988).
18. T. F. Miller and F. W. Schmidt, 'Use of a pressure-weighted interpolation method for the solution of the incompressible Navier–Stokes equations on a non-staggered grid system', *Numer. Heat Transfer*, **14**, 213–233 (1988).
19. M. H. Kobayashi and J. C. F. Pereira, 'Numerical comparison of momentum interpolation methods and pressure–velocity algorithms', *Commun. Appl. Numer. Methods*, **7**, 173–186 (1991).
20. P. J. Coelho and J. C. F. Pereira, 'Calculation of laminar recirculating flows using a local non-staggered grid refinement system', *Int. j. numer. methods fluids*, **12**, 535–557 (1991).
21. M. Peric, 'Analysis of pressure–velocity coupling on non-orthogonal grids', *Numer. Heat Transfer B*, **17**, 63–82 (1990).

22. H. L. Stone, 'Iterative solution of implicit approximations of multidimensional partial differential equation', *SIAM J. Numer. Anal.*, **5**, 530–558 (1968).
23. J. L. T. Azevedo, F. Durst and J. C. F. Pereira, 'Comparison of strongly implicit procedures for the solution of the fluid flow equations in finite-difference form', *Appl. Math. Modell.*, **12**, 51–62 (1988).
24. J. F. Thompson, Z. U. A. Warsi and C. W. Mastin, *Numerical Grid Generation—Foundations and Applications*, North-Holland, Amsterdam, 1985.
25. G. F. Almeida, D. F. G. Durão, M. V. Heitor and J. P. Simões, 'Laser–Doppler measurements of fully-development turbulent channel flow', *Proc. 5th Int. Symp. on Application of Laser Techniques to Fluid Mechanics*, Lisbon, July 1990, Paper 3.6.
26. M. C. Thompson and J. H. Ferziger, 'An adaptive multigrid technique for the incompressible Navier–Stokes equations', *J. Comput. Phys.*, **82**, 94–121 (1989).
27. D. F. G. Durão and J. C. F. Pereira, 'Calculation of isothermal turbulent three-dimensional free multi-jet flows', *Appl. Math. Model.*, **15**, 338–350 (1991).
28. V. de Brederode and P. Bradshaw, 'Influence of the side walls on the turbulent centre-plane boundary layer in a square duct', *Aero Report 75-06*, Imperial College, London, 1974.
29. P. Bradshaw, 'Turbulent secondary flows', *Ann. Rev. Fluid Mech.*, **19**, 53–74 (1987).
30. S. Obi, M. Peric and G. Scheuerer, 'A finite-volume calculation procedure for turbulent flows with second-order closure and collocated variable arrangement', *Proc. 7th Symp. on Turbulent Shear Flows*, Stanford, 1989, pp. 17.4.1–17.4.6.
31. S. Obi, M. Peric and G. Scheuerer, 'Finite-volume computation of the flow over a square rib using a second-moment turbulence closure', in W. Rodi and E. N. Ganic (eds), *Engineering Turbulence Modelling and Experiments*, Elsevier, Amsterdam, 1990, pp. 185–194.
32. J. J. McGuirk, C. Papadimitriou and A. M. K. P. Taylor, 'Reynolds stress model calculations of two-dimensional plane and axisymmetric recirculating flows', *Proc. 5th Symp. on Turbulent Shear Flows*, Davies, 1985.
33. Y. Nagano and M. Tagawa, 'An improved k–ε model for boundary layer flows', *J. Fluids Eng.*, **112**, 33–39 (1990).
34. N. N. Mansour, J. Kim and P. Moin, 'Near-wall k–ε turbulence modelling', *AIAA J.*, **27**, 1068–1073 (1989).
35. C. C. Chieng and B. E. Launder, 'On the calculation of turbulent heat transport downstream from an abrupt pipe expansion', *Numer. Heat Transfer*, **3**, 189–207 (1980).
36. B. E. Thompson and J. H. Whitelaw, 'Characteristics of a trailing-edge flow with turbulent boundary-layer separation', *J. Fluid Mech.*, **157**, 305–326 (1985).
37. Y. Morinishi and T. Kobayashi, 'Large eddy simulation of backward facing step flow', in W. Rodi and E. N. Ganic (eds), *Engineering Turbulence Modelling and Experiments*, Elsevier, Amsterdam, 1990, pp. 279–286.
38. M. A. Leschziner and W. Rodi, 'Calculation of annular and twin parallel jets using various discretization schemes and turbulence-model variations', *ASME J. Fluids Eng.*, **103**, 352–360 (1981).
39. V. de Henan, G. D. Raithby and B. E. Thompson, 'Prediction of flows with strong curvature and pressure gradient using the k–ε turbulence model', *ASME J. Fluids Eng.*, **112**, 40–47 (1990).
40. U. C. Goldberg, 'Separated flow treatment with a new turbulence model', *AIAA J.*, **24**, 1711–1713 (1986).
41. U. C. Goldberg, R. Sukumar and R. Chakravarthy, 'Prediction of separated flows with a new backflow turbulence model', *AIAA J.*, **26**, 405–408 (1988).